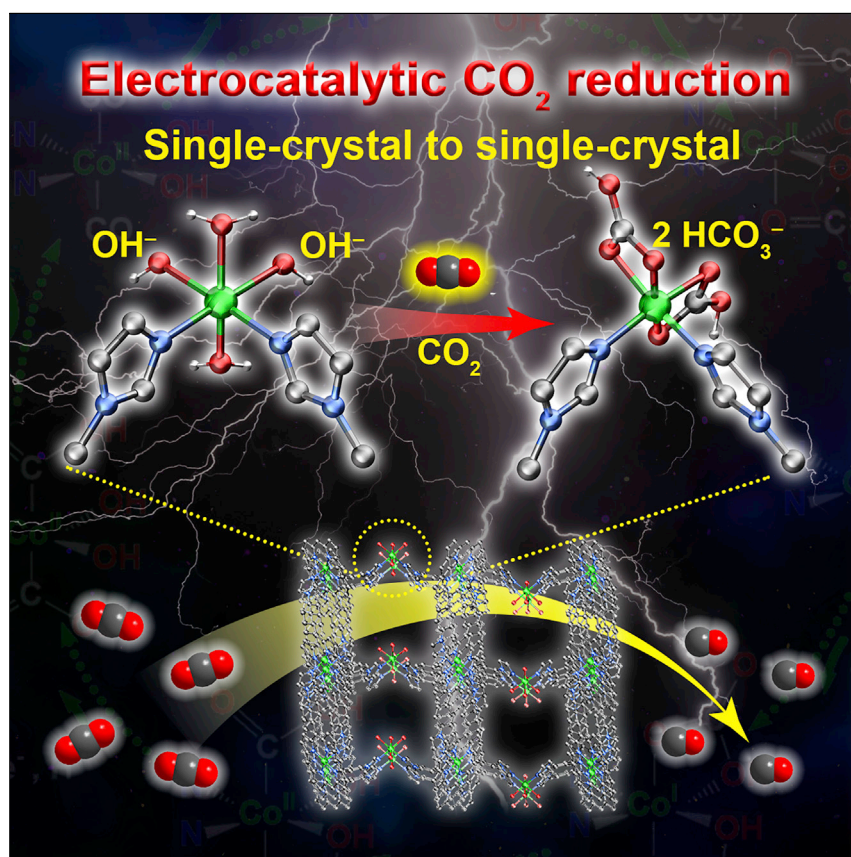


Article

Disclosing CO₂ Activation Mechanism by Hydroxyl-Induced Crystalline Structure Transformation in Electrocatalytic Process



The OH⁻-coordinated MOF was developed to simulate the surface state of catalyst in an alkaline test environment of ECR and then further explore its mechanism of CO₂ activation. It shows high faradic efficiency for CO, approximately 100%, along with long-term stability. The single-crystal to single-crystal transformation demonstrates that coordinated OH⁻ can activate the linear CO₂ into planar triangular HCO₃⁻ in the ECR process.

Qing Huang, Qiang Li, Jiang Liu, ..., Yu-Han Xia, Jin-Lan Wang, Ya-Qian Lan

yqlan@njnu.edu.cn

HIGHLIGHTS

The OH⁻-coordinated MOF shows excellent FE_{CO} with long-term stability

Coordinated OH⁻ ions cooperate with metal active center to activate CO₂ into HCO₃⁻

OH⁻-induced crystal transformation shows dynamic structural evolution of CO₂ in ECR



Benchmark

First qualification/assessment of material properties and/or performance

Huang et al., Matter 1, 1656–1668
December 4, 2019 © 2019 Elsevier Inc.
<https://doi.org/10.1016/j.matt.2019.07.003>



Article

Disclosing CO₂ Activation Mechanism by Hydroxyl-Induced Crystalline Structure Transformation in Electrocatalytic Process

Qing Huang,¹ Qiang Li,^{1,2} Jiang Liu,¹ Yi-Rong Wang,¹ Rui Wang,¹ Long-Zhang Dong,¹ Yu-Han Xia,¹ Jin-Lan Wang,² and Ya-Qian Lan^{1,3,*}

SUMMARY

The activation of CO₂ on the electrocatalyst surface is regarded as the rate-determining step in electrocatalytic CO₂ reduction (ECR), and it is therefore highly important to find out its adsorption and activation mechanism. Herein, we develop the OH[−]-coordinated metal-organic framework (NNU-15) to simulate the surface state of catalyst in alkaline environment of ECR and then further explore its activation mechanism to CO₂. NNU-15 shows high faradic efficiency for CO (FE_{CO}) reaching up to 99.2% at −0.6 V versus RHE along with long-term stability (110 h) and surpassing 96% over a wide potential range from −0.6 to −0.9 V. In the ECR process, single-crystal to single-crystal transformation between NNU-15 and NNU-15-CO₂ demonstrates that coordinated OH[−] can activate the CO₂ into HCO₃[−], which will chelate to the metal center. Theoretical calculations validate that both O-adsorbed and C-adsorbed initial geometries are inclined to result in the formation of HCO₃[−] during the ECR process.

INTRODUCTION

Converting atmospheric excess carbon dioxide (CO₂) into chemical feedstock or low-carbon fuel is not only beneficial for mitigating the greenhouse effect but also to some extent for alleviating the energy crisis.^{1–4} Electroreduction of CO₂ is regarded as a promising strategy^{4–7} featuring (1) controllability of the voltage during the reaction process, (2) recyclability of electrolyte, (3) a sustainable source of electrical energy, and (4) a well-knit reaction system. The ECR process includes three main steps:^{5,8–11} (1) adsorption of CO₂ on the catalyst for CO₂* formation; (2) electron transfer and proton migration for cleaving the C=O bond and producing C–O and/or C–H bonds; and (3) desorption and diffusion of conversion products from the catalyst surface. Among of them, the first step is the main and key step for ECR, as it requires a large amount of reorganizational energy to adsorb and activate linear CO₂ molecules to form CO₂*, occurring at −1.90 V versus standard hydrogen electrode.¹² The current study of ECR mechanism focuses on various products that involve generation of different intermediates (e.g., *COOH, *OCCOH, *CO)^{10,13–17} relating to several proton-coupled electron transfer steps based on CO₂*;¹⁸ by contrast, few have been committed to revealing the most important process of CO₂ adsorption and activation. Therefore, it is of great significance to design and develop suitable ECR catalysts for the investigation and elucidation of the adsorption and activation mode of CO₂.

The current reported ECR electrocatalysts are mainly concentrated on nanocatalysts.^{19–23} Some strategies have been adopted to improve the performance of

Progress and Potential

Electrocatalytic CO₂ reduction (ECR) is an effective method to convert CO₂ into energy products by means of efficient electrocatalysts. In the ECR process, the first step requires a large reorganizational energy to adsorb and activate linear CO₂ molecules, which is the most crucial step for ECR. A clear CO₂ activation mechanism is extremely important for investigating the mechanism of different reduction products, and developing efficient target catalysts to improve the ECR performance. Herein, we design and report a stable OH[−]-coordinated metal-organic framework as catalyst model to investigate the CO₂ activation mechanism in the ECR process. The capture of OH[−]-induced single-crystal to single-crystal transformation in ECR clearly expresses the dynamic structural evolution (CO₂-HCO₃[−]) of CO₂ in the electrocatalytic process, providing profound evidence to help disclose the CO₂ activation mechanism.

electrocatalysts, such as increasing the specific surface area of catalysts,²⁴ modulating the dispersion of the catalytic center (e.g., single-atom catalyst and atom-pair catalyst),^{25,26} and especially introducing the oxygen vacancies (V_{Os}) and surface defects into some nanocatalysts.²⁷ For heterogeneous catalysts, some molecules or ions in solution can directly interact with the surface defect sites or V_{Os} to improve the activity of catalysts, which leads to the remarkable results in electrocatalytic hydrogen evolution reaction,²⁸ oxygen evolution reaction,²⁹ and methanol oxidation reaction.³⁰ However, there are still many problems while these methods are being utilized in N_2 or CO_2 reduction processes due to the gas as the reactant in three-phase (solid, gas, and liquid) reactions, since the created defect sites or V_{Os} tend to be coordinated or interacted with the large number of liquid molecules or ions rather than the gas molecules in solution during the reaction process.^{31–33} Thus, adsorption and activation of CO_2 on the catalyst surface, the rate-determining step of ECR, may not be just affected by the interaction between CO_2 and metal sites, but also the strength of the interaction between CO_2 and ions/small molecules of solution that can coordinate on the metal surface and determine the CO_2 adsorption and activation capacity of the catalyst. Most heterogeneous catalysts for ECR have no precise molecular structure. Even with many *in situ* characterizations,^{21,34} it is still difficult to provide intuitive and accurate evidence of the catalytic mechanism of ECR, especially regarding the mode for CO_2 chemisorption and activation.

Metal-organic frameworks (MOFs),^{35–38} which are open frameworks, have emerged as a promising electrocatalyst for ECR due to their high CO_2 adsorption⁷ and clear metal active sites.^{39–42} Some MOFs have been used in ECR,⁴³ such as HKUST-1,^{42,44} CR-MOF,⁴⁵ $\text{Al}_2(\text{OH})_2(\text{Co}(\text{tcpp}))$,⁴⁰ and Fe-MOF-525,⁴⁶ but the faradic efficiency and long-term stability still need to be improved. Furthermore, MOFs with accurate structure can be modulated with small molecules/ions coordination on the metal center, promoting the study of the effects of small molecules/ions in ECR reactions, which is very important for the ECR mechanism. The development of stable MOFs with high selectivity and remarkable activity toward CO_2 reduction and the related investigation of ECR mechanism has become our target task.

Herein, we design and report a stable MOF with two OH^- ions [NNU-15, $\text{Co}(\text{OH})_2(\text{H}_2\text{O})_2(\text{Co-TIPP})$] composed of Co^{II} ions and TIPP linkers to act as a crystal model for simulating the surface state of catalyst in an alkaline test environment of ECR, and further explore its adsorption and activation mechanism with CO_2 . The TIPP ([5,10,15,20-tetra(4-imidazol-1-yl)phenyl]porphyrin) ligand decorated by the imidazole group can be used to construct more stable MOFs.⁴⁷ Besides, the TIPP ligand including the porphyrin moiety is considered to be beneficial for efficient electron conduction, further facilitating the construction of efficient MOF catalysts for electrochemical applications.⁴⁸ Moreover, as a neutral ligand, TIPP is also propitious for the counterbalanced coordination between other anions and the metal center, making it possible to obtain the MOF crystal model with OH^- coordination to uncover the ECR mechanism under a simulated alkaline environment (most ECR occurs in alkaline conditions). Indeed, the NNU-15 crystal bearing OH^- coordinated the open Co-active site exhibits high faradic efficiency for CO (FE_{CO}), reaching up to 99.2% at a low potential (-0.6 V versus reversible hydrogen electrode [RHE]) along with long-term stability (110 h) and surpassing 96% in a wide potential (-0.6 V to -0.9 V), which betters all reported MOF-based electrocatalysts. A major discovery is that the accurate structure of NNU-15- CO_2 has been obtained in the ECR process, which reveals that OH^- can cooperate with the Co-active center of NNU-15 to capture CO_2 and activate it to create HCO_3^- . The HCO_3^- will chelate the metal active center, giving rise to NNU-15- CO_2 . Lee et al. considered that HCO_3^- is an important

¹Jiangsu Collaborative Innovation Centre of Biomedical Functional Materials, Jiangsu Key Laboratory of New Power Batteries, School of Chemistry and Materials Science, Nanjing Normal University, Nanjing 210023, P. R. China

²School of Physics, Southeast University, Nanjing 211189, P. R. China

³Lead Contact

*Correspondence: yqlan@njnu.edu.cn

<https://doi.org/10.1016/j.matt.2019.07.003>

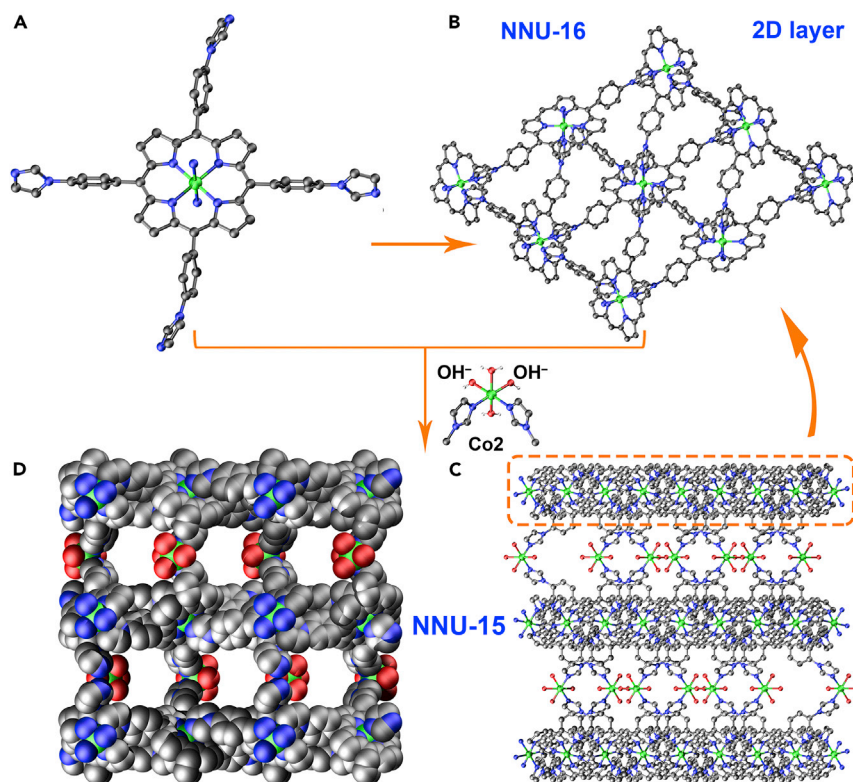


Figure 1. Crystal Structures of NNU-15 and NNU-16

Color code: C, black; N, blue; O, red; Co, green. Symmetry codes: #1 $0.5 - x, -0.5 + y, 0.5 - z$; #2 $0.5 + x, 0.5 - y, 0.5 + z$; #3 $1 - x, -y, 1 - z$.

(A) Coordination of Co1 ion in NNU-15 or NNU-16.

(B) 2D layer (NNU-16).

(C) 3D frameworks for NNU-15 along the b axis.

(D) 3D frameworks with open hole in NNU-15.

intermediate in the ECR process,⁴⁹ and fourier-transform infrared (FTIR) spectroscopy showed that CO_2 could be activated to form HCO_3^- in alkaline solution.⁵⁰ Fortunately, the generated NNU-15- CO_2 intermediate could be captured to further provide powerful evidence of the coordinated OH^- participation mechanism in the ECR process. Furthermore, we demonstrate that the coordinated OH^- on the metal active center is significant for CO_2 chemisorption, and its transfer into HCO_3^- may be a necessary pathway for ECR to further enhance ECR performance under alkaline conditions.

RESULTS AND DISCUSSION

Structure and Characterization of the MOFs

Single crystals of NNU-15 were synthesized by solvothermal synthesis (see [Experimental Procedures](#)). Single-crystal X-ray diffraction (XRD) analysis reveals that the as-prepared NNU-15 crystallizes in the orthorhombic *Pnma* space group (Table S1). Each Co1 ion trapped in the TIPP center coordinates two N atoms of imidazole from TIPP ligands to form a 2D layer (Figures 1A and 1B). The Co2 ion connects two N atoms of imidazole, two OH^- , and two H_2O molecules (Figure S2). Adjacent porphyrin layers are linked by Co2 ions to generate the 3D opening framework of NNU-15 (Figure 1), while NNU-16 (formulated as Co-TIPP, Table S1) employs two imidazoles to connect neighboring Co1 ions of the TIPP center, fabricating a 2D

porphyrin layer (Figures 1A and 1B). Both NNU-15 and NNU-16 employ TIPP ligands to coordinate with Co ions, but the main difference is that NNU-16 lacks the OH⁻-coordinated Co2 site compared with NNU-15.

The consistency between the powder X-ray diffraction (PXRD) patterns of as-synthesized crystals and the simulated PXRD pattern demonstrates the high purity of NNU-15 and NNU-16 (Figures S3 and S4). NNU-15 exhibits good thermal stability under O₂ atmosphere according to thermogravimetric analysis (TGA) results (Figure S5). For NNU-15, the CO₂ uptake was determined to be 48 cm³ g⁻¹ at 298 K, and the desorption process became sluggish due to strong CO₂ adsorption (Figure S6).

Performance on Electrocatalytic CO₂ Reduction

The linear sweep voltammetry (LSV) experiments were conducted to measure the electrocatalytic reduction of CO₂ for catalysts. The small onset potential located at -0.36 V for NNU-15 is much more positive than that of NNU-16 (-0.50 V) and TIPP ligand (-0.80 V) (Figure 2A) under saturated CO₂ atmosphere. Moreover, the current density of NNU-15 (32.2 mA cm⁻²) is much higher than that of NNU-16 (20.5 mA cm⁻²) and TIPP ligand (22.1 mA cm⁻²) at -1.1 V (Figure 2A). A much lower current density under saturated Ar atmosphere was obtained compared with CO₂ atmosphere, which indicated that NNU-15 is capable of CO₂ electroreduction (Figure S7).

To obtain insight into the performance for ECR, we carried out faradic efficiency (FE) experiments to assess the selectivity for CO₂ conversion. CO and H₂ are the main reduction products by gas chromatography (GC) detector analysis (Figure S8). FE_{CO} and FE_{H₂} were recorded over the entire potential range from -0.5 V to -1.0 V (Figures 2B, S9, and S10). The result of ¹H nuclear magnetic resonance (NMR) spectroscopy reveals that there is no liquid product recorded (Figure S11). NNU-15 is highly selective and active for converting CO₂ into CO, approaching a high FE_{CO} above 96% in a wide potential ranging from -0.6 V to -0.9 V and a maximum FE_{CO} (99.2%) at -0.6 V, while NNU-16 and TIPP ligand exhibit maximum FE_{CO} of 50.7% and 9.1% at -0.8 V and -0.7 V, respectively (Figures 2B and 2C). Moreover, at -0.6 V the FE_{CO} (99.2%) of NNU-15 surpasses that of NNU-16 (26.9%) and TIPP (3.6%) (Figure S12). Compared with TIPP ligand and NNU-16, the excellent ECR selectivity for NNU-15 is mainly attributed to the active Co2 site. By contrast, NNU-16 without Co2 site and free TIPP ligand has relatively poor performance. Furthermore, such a wide potential range (-0.6 to -0.9 V) associated with high FE_{CO} surpasses that of many reported materials, and the low potential (-0.6 V) corresponding to the maximum FE_{CO} is smaller than that of many MOF-based materials (Table S2). At -0.6 V, the turnover frequency of NNU-15 (37.5 h⁻¹) is also higher than that of NNU-16 (5.3 h⁻¹) (Table S2 and Figure S13). Moreover, under 10% concentration of CO₂ atmosphere (simulating flue gas concentration), the maximum FE_{CO} of NNU-15 can also reach up to 70.2% at -0.7 V, which indicates that NNU-15 possesses outstanding capacities to capture and activate CO₂ (Figures 2D and S14).

The electrochemical active surface area (ECSA) is identified by electrochemical double-layer capacitance (C_{dl}) obtained from cyclic voltammogram (CV) curves to reveal the excellent performance of NNU-15. As shown in Figure S15, C_{dl} of NNU-15 is calculated to be 5.88 mF cm⁻², superior to that of NNU-16 (4.21 mF cm⁻²) and TIPP ligand (3.26 mF cm⁻²), suggesting that the larger available area of NNU-15 provides more active sites to promote ECR. The partial current densities for CO (j_{CO}) and H₂ (j_{H₂}) illustrate that the effective current density of NNU-15 is superior to that of the

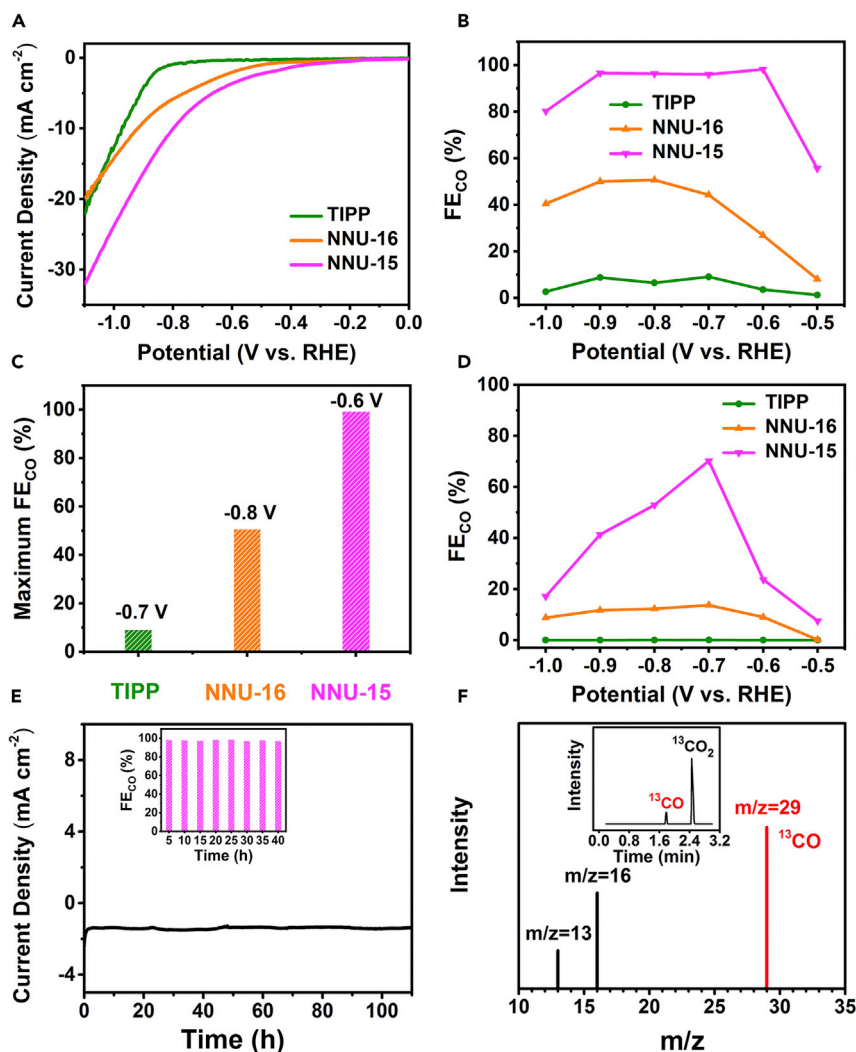


Figure 2. Electrocatalytic Performances of MOFs

(A) Linear sweep voltammetric curves.

(B) Faradic efficiencies for CO.

(C) Maximum FE_{CO} of TIPP (−0.7 V), NNU-16 (−0.8 V), and NNU-15 (−0.6 V).

(D) The faradic efficiencies for CO were measured in 10% concentration of CO₂ atmosphere (simulating flue gas concentration).

(E) Durability test of NNU-15 at the potential of −0.6 V versus RHE.

(F) Gas chromatography and mass spectra of ¹³CO recorded under a ¹³CO₂ atmosphere.

Except for (D), tests were performed in 0.5 M KHCO₃ electrolyte with saturated CO₂ atmosphere (99.999%).

comparison samples (Figure S16). Moreover, as Tafel slopes illustrate, the slope of NNU-15 is 183 mV dec⁻¹, which is lower than that of NNU-16 (190 mV dec⁻¹) and TIPP ligand (194 mV dec⁻¹), indicating the fastest reaction rate on NNU-15 (Figure S17). Furthermore, electrochemical impedance spectroscopy (EIS) experiments were performed to investigate the kinetics for ECR. The charge-transfer resistance of NNU-15 is much smaller than that of the other two counterparts, indicating the faster shuttling of charge transfers during the ECR process on NNU-15. The enhanced charge-transfer rate could enable minimized parasitic ohmic losses and contribute to the remarkably raised selectivity and activity toward CO₂ electroreduction (Figure S18).

Long-term stability of the catalyst is one of the major challenges for electrocatalytic reduction of CO₂. The current density remains stable over 2.7 mA cm⁻² after 110 h and the FE_{CO} could be kept above 96% after 40 h by detecting the products every 5 h, which demonstrates that there is no obvious decline of selectivity and activity of NNU-15 during the CO₂ reduction process (Figure 2E). Besides, inductively coupled plasma emission spectrometry (ICP) and UV-visible (UV-vis) spectroscopy demonstrate that nothing dissolves after testing (Table S3 and Figure S19). These stability detections reveal that NNU-15 is an extremely stable and promising catalyst in ECR reactions. Finally, an isotopic experiment was conducted under ¹³CO₂ atmosphere to validate the carbon source of the products, and the generated gases were analyzed by GC-mass spectrometry (MS). The peak at *m/z* = 29 is assigned to ¹³CO, providing strong evidence that NNU-15 as electrocatalyst indeed has the activity and selectivity necessary to convert CO₂ into CO (Figure 2F).

Disclosing CO₂ Activation Mechanism by OH⁻-Induced Crystalline Structure Transformation

To disclose the origin and difference of ECR performance for NNU-15 and NNU-16, we mainly consider the structural fragments of Co1-TIPP and the Co2 site. NNU-16 with Co1 at the TIPP center exhibits poor performance, because the Co1 coordinated with 6 N atoms becomes less attractive to CO₂. Moreover, NNU-16 can be regarded as one layer of NNU-15 (Figures 1B and 1C), and the ECR performance of NNU-15 is significantly enhanced compared with NNU-16, mainly attributable to the Co2 subunit. To study the effect of OH⁻ ions coordinated to the Co2 site on ECR performance, we carried out PXRD patterning after the ECR experiment. A shift toward a higher 2θ region of the peak at around 7.76° is obtained compared with the original one (Figures S20 and 3C). To verify whether a new substance was produced, the NNU-15 crystals were soaked in the simulated ECR environment. After 20 h, we found that the PXRD pattern of these infiltrated crystals had also changed and were consistent with those after the ECR reaction. The marinated crystals were characterized by single-crystal XRD. PXRD patterns and single-crystal XRD analysis demonstrate that the NNU-15 has transferred into NNU-15-CO₂ under simulated alkaline conditions. Fortunately, we obtained the well-defined crystal structure of NNU-15-CO₂ after the ECR reaction, and it crystallizes in the orthorhombic *P*2₁2₁2₁ space group (Table S1). Each Co2 ion cooperating with two OH⁻ ions of NNU-15 captures CO₂ molecules to form two HCO₃⁻ groups of NNU-15-CO₂ (Figures 3A and 3B). There is no obvious valence-state difference for Co(II) in NNU-15 and NNU-15-CO₂ via X-ray photoelectron spectroscopy analysis (Figure S21). Furthermore, the structural changes of NNU-15 related to time are provided in Figure S22. There existed a single-crystal to single-crystal transformation from NNU-15 to NNU-15-CO₂, and the NNU-15 fully turned into NNU-15-CO₂ after reaction time of 4 h.

The PXRD pattern of the catalyst after the ECR reaction is consistent with that of NNU-15-CO₂, which proves that NNU-15-CO₂ is a relatively stable intermediate in the ECR process (Figure S20). After reaction the crystal morphology remained unchanged, but its surface became a little smooth. Scanning electron microscopy results also indicated that surface catalysis does occur on NNU-15 in the ECR process, in which case the NNU-15 has converted into NNU-15-CO₂ (Figure S23). Furthermore, NNU-15 has been demonstrated to be easily adsorbed by CO₂ to form bicarbonate-chelated NNU-15-CO₂ due to the participation of coordinated OH⁻. In addition, NNU-15 can also capture traces of CO₂ to change into NNU-15-CO₂ when exposed to alkaline solution or air (Figure 3D), considering that the majority of ECR experiments are commonly performed under alkaline conditions, whereby the amount of OH⁻ ions are supposed to be dominant. When the catalyst is soaked

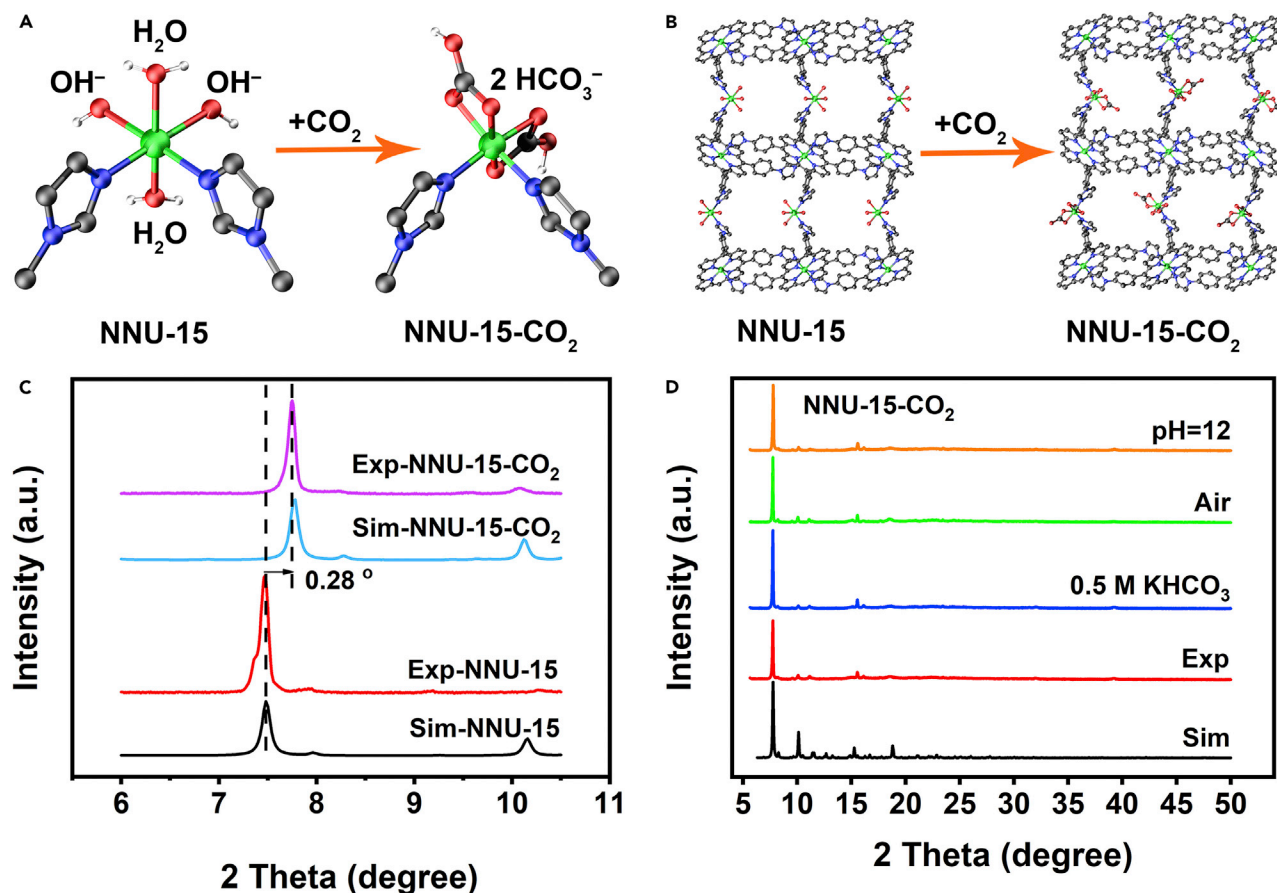


Figure 3. NNU-15 Changed into NNU-15-CO₂ in ECR Process

(A) Co₂ section of NNU-15-adsorbed CO₂ to form NNU-15-CO₂.

(B) 3D frameworks, NNU-15-adsorbed CO₂ to form NNU-15-CO₂.

(C) PXRD difference between NNU-15 and NNU-15-CO₂. "Sim": simulated pattern and "Exp": as-synthesized sample.

(D) NNU-15 crystals were soaked in the simulated ECR conditions (0.5 M KHCO₃), as well as in air and alkaline conditions, and the traces of CO₂ to form NNU-15-CO₂ were captured.

in electrolyte for ECR, the negatively charged OH⁻ ions are more competitive than other neutral solvent molecules in coordinating with the positively charged metal active center. In this case, the coordinated OH⁻ ions are very likely to play a crucial role in activating the absorbed CO₂ molecule. In particular, the capture of OH⁻-induced single-crystal to single-crystal transformation from NNU-15 to NNU-15-CO₂ in ECR clearly expresses the dynamic structural evolution (CO₂→HCO₃⁻) of CO₂ in the electrocatalytic process, providing profound evidence to help disclose the CO₂ activation mechanism.

DFT Calculations

Density functional theory (DFT) calculations were further performed to identify the active sites and reveal the catalytic reaction mechanisms of ECR. A cluster model was applied for all the calculations and the long-range interactions were neglected. The whole NNU-15 structure is divided into two separate fragments, in which the metals are treated as catalytic centers, and we term these two fragments Co1 and Co2. In the case of porphyrin fragment, the Co1 sites are saturated with six N atoms from TIPP ligands; thus, the attraction for CO₂ from the metals is limited due to the



Matter 1, 1656–1668, December 4, 2019 1663

shown in Figure S26 and Table S4. DFT calculation results show that both O-adsorbed and C-adsorbed initial geometries are inclined to form HCO_3^- and further reveal the adsorption mode of CO_2 whereby the coordinated OH^- ions cooperate with the metal active center to capture CO_2 into HCO_3^- . Such formation of HCO_3^- is the result of CO_2 chemisorption and activation in ECR, which is consistent with the experimental results.

Conclusion

In summary, NNU-15 with two coordinated OH^- ions was reported and used as a crystalline model to investigate the adsorption and activation mode of CO_2 in the ECR reaction. NNU-15, acting as an electrocatalyst, exhibits high FE_{CO} at a low potential (99.2% at -0.6 V) along with long-term stability (110 h), even in a wide potential range from -0.6 V to -0.9 V, with high FE_{CO} (over 96%). Even under 10% concentration of CO_2 atmosphere (simulating flue gas concentration), the maximum FE_{CO} can also reach up to 70.2% at -0.7 V, indicating that NNU-15 possesses outstanding ability to capture and convert the CO_2 molecule. Such excellent performances have surpassed those of all the reported MOF-based electrocatalysts applied to ECR. In the ECR process, we obtained the intermediate (NNU-15- CO_2 with well-defined crystal structure), which demonstrated that the metal catalytic center of MOF can cooperate with OH^- to capture and activate the CO_2 molecule to form the HCO_3^- -chelating metal active center. Moreover, single-crystal to single-crystal transformation between NNU-15 and NNU-15- CO_2 in ECR provides solid evidence to help disclose the CO_2 activation mechanism. DFT calculations further show that both O-adsorbed and C-adsorbed initial geometries are inclined to form HCO_3^- due to the participation of OH^- ions. Both experimental results and DFT calculations demonstrate that the coordinated OH^- on the metal active center is significant for CO_2 chemisorption and activation, and the formation of HCO_3^- may be a necessary pathway for the ECR mechanism under alkaline conditions. This important discovery may modulate the future research emphasis on the ECR mechanism involving the participation of OH^- ions for various catalytic materials and dramatically promote the progress of ECR.

EXPERIMENTAL PROCEDURES

Synthesis of NNU-15 and NNU-16

All chemicals and reagents were obtained from commercial sources. TIPP (11 mg, 0.013 mmol) and $\text{CoCl}_2 \cdot 6\text{H}_2\text{O}$ (47.6 mg, 0.20 mmol) were dissolved in the mixed solvent ($\text{DMF}/\text{H}_2\text{O} = 5:1$, $V = 6$ mL) and stirred for 10 min. This mixture was sealed and heated at 120°C for 72 h. Purple flaky crystals of NNU-15 were isolated and collected (71% yield based on TIPP). TIPP (22 mg, 0.025 mmol) and $\text{CoCl}_2 \cdot 6\text{H}_2\text{O}$ (47.6 mg, 0.20 mmol) were dissolved in the mixed solvent ($\text{DMF}/\text{H}_2\text{O} = 1:1$, $V = 6$ mL). This mixture was stirred for 10 min and sealed in a 10-mL glass vial, then kept at 120°C for 72 h. After cooling to room temperature at $10^\circ\text{C}/\text{h}$, violet crystal samples of NNU-16 were obtained and isolated (55% yield based on TIPP). Infrared spectra were recorded and are shown in Figure S27. CCDC numbers: 1874634 (NNU-15), 1891188 (NNU-15- CO_2), and 1874635 (NNU-16). CCDC: 1874634, 1891188, 1874635.

Single-Crystal X-Ray Crystallography

Single-crystal XRD data collection for NNU-15 was measured on a Bruker APEXII CCD diffractometer (graphite-monochromated $\text{Mo K}\alpha$ radiation, $\lambda = 0.71073$ Å) at 296 K. NNU-15- CO_2 and NNU-16 were measured on an SSRF BL17B diffractometer at the National Facility for Protein Science Shanghai at 100 K. All of them were solved using direct methods by SHELXT and refined by the SHELXL-2014 program within

Olex². Anisotropic temperature parameters were used to refine all nonhydrogen atoms. Hydrogen atoms were located at calculated positions. NNU-15, NNU-16, and NNU-15-CO₂ were corrected with the SQUEEZE program and a part of PLATON software was utilized to check the space group of crystal owing to solvent molecule disorder. Crystallographic data for NNU-15, NNU-16, and NNU-15-CO₂ are summarized and shown in Table S1.

Characterizations and Instruments

Infrared spectra ranging from 4,000 to 400 cm⁻¹ were recorded on a Bruker Tensor 27 FTIR spectrophotometer utilizing KBr pellets. TGA was performed on a Netzsch STA449F3 analyzer under an oxygen atmosphere from room temperature to 700°C (heating rate 10°C min⁻¹). PXRD data (6°–50°) were collected by a D/max 2500VL/PC diffractometer equipped with graphite monochromatized Cu K α radiation (λ = 1.54060 Å).

Electrochemical Measurements

All electrocatalysis tests of these catalysts were carried out on the electrochemical workstation (Bio-Logic) using the standard three-electrode configuration (Ag/AgCl electrode and Pt wire acted as the reference and counter electrode, respectively) in an airtight H-type cell injected with 0.5 M KHCO₃ (pH 7.2). The total volume of the H-type cell is 100 mL (50 mL on each side). To enhance the conductivity of the MOF catalysts, we introduced acetylene black (AB) into the pure MOF crystals by grinding the mixture. In many reported works, Nafion solution as a dispersion solution was generally employed to form a uniform ink with MOF and AB, which was propitious in attaching to the surface of carbon paper. The preparation process of the working electrode is as follows. Ten milligrams of AB and 10 mg of pure MOF crystal as catalyst were ground uniformly, and 0.5% Nafion solution (1,000 μ L) added. The catalysts were ground by the ball mill for 3 min with 60 Hz s⁻¹, and the influences of grinding time were considered (Figure S28). After grinding for 1 min, the maximum FE_{CO} is 88.1% when the obtained catalyst particles are relatively large. The particle size obtained is similar in both cases where the catalyst samples were ground for 3 min and 5 min, and both the obtained catalyst particles are optimal for ECR performance with FE_{CO} of approximately 100% at -0.6 V versus RHE. These results demonstrated that the size of the catalyst particles does have an effect on performance, and the best ECR performance can be obtained when catalyst particles reach a certain size after grinding. For an even mix, the mixture requires sonication for 30 min. The mixture was then dropped on carbon paper (1 cm \times 1 cm) with MOF loading density of about 1 mg cm⁻². After natural drying, the working electrode (total area, 1 cm \times 2 cm) could be used for testing.

At a scan rate of 5 mV s⁻¹, LSV mode was utilized to obtain the polarization curves in ECR experiments. The polarization curves of the working electrode were recorded under inert atmosphere (Ar gas) and CO₂ (99.999%), respectively. The FE experiments were performed from -0.5 V to 1.0 V (versus RHE) in 0.5 M KHCO₃ solution (both the cathode and the anode contain 25 mL), bubbling with CO₂ (99.999%) atmosphere for about 40 min until the pressure relief valve displayed 0.5 MPa. The calculations for FE of catalysts are shown in Supplemental Information. Both carbon paper and AB have a low current density and produce hydrogen gas rather than CO over the potential range (-0.5 V to -1.0 V versus RHE), which certifies that the outstanding performance stems from the catalyst activity (Figures S29 and S30). In addition, in 10% concentration of CO₂ atmosphere instead of the CO₂ (99.999%), the FE experimental conditions are similar. Based on the Nernst equation E (versus RHE) = E (versus Ag/AgCl) + 0.1989V + 0.059 \times pH, the test results were reported

versus RHE. To evaluate ECSA, we recorded the double-layer capacitance (C_{dl}) by CVs with various scan rates from 20 to 200 mV s^{-1} . EIS experiments executed ranged from 1,000 kHz to 0.1 Hz at an overpotential (-0.6 V versus RHE) using an AC voltage with 10 mV amplitude.

Detection of Products

The generated gaseous products were analyzed by a gas chromatograph (GC-7900, CEAULIGHT, China) equipped with a flame ionization detector and thermal conductivity with helium as carrier gas. The generated gas was analyzed offline by injection into the gas chromatograph after collecting the generated gas. Details are as follows. When the reaction reached about 5 coulombs, we utilized gas-tight syringes (Hamilton) to inject 500 μL into the gas chromatograph, and calculated the FE according to the formula in [Supplemental Information](#). The results of isotope-labeled experiments ($^{13}\text{CO}_2$ instead of CO_2) were analyzed by GC-MS (7890A and 5875C, Agilent). After the reaction, the liquid products were collected and quantified by an NMR spectroscope (Bruker AVANCEAV III 400). The specific operation is as follows: 0.5 mL of electrolyte after reaction (0.6 V) was mixed with 0.1 μL of dimethyl sulfoxide (99.99%, internal standard) and 0.1 mL of D_2O . A solvent presaturation technique was implemented to suppress the water peak. The UV-vis spectra were recorded on a UV-vis instrument (Beijing Purkinje, TU-1900). The ICP results after reactions were measured on ICPOES (Agilent 720) and ICPMS (Agilent 7700).

SUPPLEMENTAL INFORMATION

Supplemental Information can be found online at <https://doi.org/10.1016/j.matt.2019.07.003>.

ACKNOWLEDGMENTS

This work was financially supported by NSFC (nos. 21622104, 21871141, 21871142, and 21701085), the NSF of Jiangsu Province of China (no. SBK2017040708), the Natural Science Research of Jiangsu Higher Education Institutions of China (no. 17KJB150025), Postgraduate Research & Practice Innovation Program of Jiangsu Province (KYCX18_1189), Priority Academic Program Development of Jiangsu Higher Education Institutions, and the Foundation of Jiangsu Collaborative Innovation Center of Biomedical Functional Materials. We thank the staff from BL17B at Shanghai Synchrotron Radiation Facility for assistance during data collection.

AUTHOR CONTRIBUTIONS

Y.-Q.L. and Q.H. conceived and designed the project. Q.H. and Y.-R.W. performed the experiments, and collected and analyzed the data. Q.L. and J.-L.W. performed the DFT calculations. Q.H., J.L., and Y.-Q.L. co-revised the paper. L.-Z.D., R.W., and Y.-H.X. assisted with the experiments and characterizations. All authors discussed the results and commented on the manuscript.

DECLARATION OF INTERESTS

The authors declare no competing interests.

Received: May 3, 2019

Revised: June 13, 2019

Accepted: July 9, 2019

Published: September 11, 2019

REFERENCES

- Liu, C., Colón, B.C., Ziesack, M., Silver, P.A., and Nocera, D.G. (2016). Water splitting-biosynthetic system with CO₂ reduction efficiencies exceeding photosynthesis. *Science* 352, 1210–1213.
- Wu, J., Huang, Y., Ye, W., and Li, Y. (2017). CO₂ reduction: from the electrochemical to photochemical approach. *Adv. Sci.* 4, 1700194.
- Jouny, M., Luc, W., and Jiao, F. (2018). High-rate electroreduction of carbon monoxide to multi-carbon products. *Nat. Catal.* 1, 748–755.
- Weekes, D.M., Salvatore, D.A., Reyes, A., Huang, A., and Berlinguette, C.P. (2018). Electrolytic CO₂ reduction in a flow cell. *Acc. Chem. Res.* 51, 910–918.
- Wang, Y., Han, P., Lv, X., Zhang, L., and Zheng, G. (2018). Defect and interface engineering for aqueous electrocatalytic CO₂ reduction. *Joule* 2, 1–32.
- Won, D.H., Shin, H., Koh, J., Chung, J., Lee, H.S., Kim, H., and Woo, S.I. (2016). Highly efficient, selective, and stable CO₂ electroreduction on a hexagonal Zn catalyst. *Angew. Chem. Int. Ed.* 55, 9297–9300.
- Bien, C.E., Chen, K.K., Chien, S.C., Reiner, B.R., Lin, L.C., Wade, C.R., and Ho, W.S.W. (2018). Bioinspired metal-organic framework for trace CO₂ capture. *J. Am. Chem. Soc.* 140, 12662–12666.
- Zhu, D.D., Liu, J.L., and Qiao, S.Z. (2016). Recent advances in inorganic heterogeneous electrocatalysts for reduction of carbon dioxide. *Adv. Mater.* 28, 3423–3452.
- Gong, J., Zhang, L., and Zhao, Z.J. (2017). Nanostructured materials for heterogeneous electrocatalytic CO₂ reduction and related reaction mechanisms. *Angew. Chem. Int. Ed.* 56, 11326–11353.
- Handoko, A.D., Wei, F., Jenndy, Yeo, B.S., and Seh, Z.W. (2018). Understanding heterogeneous electrocatalytic carbon dioxide reduction through operando techniques. *Nat. Catal.* 1, 922–934.
- Zheng, Y., Vasileff, A., Zhou, X., Jiao, Y., Jaroniec, M., and Qiao, S.-Z. (2019). Understanding the roadmap for electrochemical reduction of CO₂ to multi-carbon oxygenates and hydrocarbons on copper-based catalysts. *J. Am. Chem. Soc.* 141, 7646–7659.
- Benson, E.E., Kubiak, C.P., Sathrum, A.J., and Smieja, J.M. (2008). Electrocatalytic and homogeneous approaches to conversion of CO₂ to liquid fuels. *Chem. Soc. Rev.* 38, 89–99.
- Zhao, C.X., Bu, Y.F., Gao, W., and Jiang, Q. (2017). CO₂ reduction mechanism on the Pb(111) surface: effect of solvent and cations. *J. Phys. Chem. C* 121, 19767–19773.
- Pérez-Gallent, E., Figueiredo, M.C., Calle-Vallejo, F., and Koper, M.T. (2017). Spectroscopic observation of a hydrogenated CO dimer intermediate during CO reduction on Cu(100) electrodes. *Angew. Chem. Int. Ed.* 129, 3675–3678.
- Cheng, T., Xiao, H., and Goddard, W.A. (2016). Reaction mechanisms for the electrochemical reduction of CO₂ to CO and formate on the Cu(100) surface at 298K from quantum mechanics free energy calculations with explicit water. *J. Am. Chem. Soc.* 138, 13802–13805.
- Vasileff, A., Xu, C., Jiao, Y., Zheng, Y., and Qiao, S.-Z. (2018). Surface and interface engineering in copper-based bimetallic materials for selective CO₂ electroreduction. *Chem* 4, 1809–1831.
- Jiao, Y., Zheng, Y., Chen, P., Jaroniec, M., and Qiao, S.Z. (2017). Molecular scaffolding strategy with synergistic active centers to facilitate electrocatalytic CO₂ reduction to hydrocarbon/alcohol. *J. Am. Chem. Soc.* 139, 18093–18100.
- Zhuang, T.-T., Liang, Z.-Q., Seifitokaldani, A., Li, Y., De Luna, P., Burdyny, T., Che, F., Meng, F., Min, Y., Quintero-Bermudez, R., et al. (2018). Steering post-C-C coupling selectivity enables high efficiency electroreduction of carbon dioxide to multi-carbon alcohols. *Nat. Catal.* 1, 421–428.
- Kim, D., Xie, C., Becknell, N., Yu, Y., Karamad, M., Chan, K., Crumlin, E.J., Nørskov, J.K., and Yang, P. (2017). Electrochemical activation of CO₂ through atomic ordering transformations of AuCu nanoparticles. *J. Am. Chem. Soc.* 139, 8329–8336.
- Wenlei, Z., Ronald, M., Onder, M., Haifeng, L., Shaojun, G., Wright, C.J., Xiaolian, S., Peterson, A.A., and Shouheng, S. (2013). Monodisperse Au nanoparticles for selective electrocatalytic reduction of CO₂ to CO. *J. Am. Chem. Soc.* 135, 16833–16836.
- Luna, P.D., Quintero-Bermudez, R., Dinh, C.T., Ross, M.B., Bushuyev, O.S., Todorović, P., Regier, T., Kelley, S.O., Yang, P., and Sargent, E.H. (2018). Catalyst electro-redeposition controls morphology and oxidation state for selective carbon dioxide reduction. *Nat. Catal.* 1, 103–110.
- Lu, Q., Rosen, J., Zhou, Y., Hutchings, G.S., Kimmel, Y.C., Chen, J.G., and Jiao, F. (2014). A selective and efficient electrocatalyst for carbon dioxide reduction. *Nat. Commun.* 5, 3242.
- Vasileff, A., Zheng, Y., and Qiao, S.Z. (2017). Carbon solving carbon's problems: recent progress of nanostructured carbon-based catalysts for the electrochemical reduction of CO₂. *Adv. Energy Mater.* 7, 1700518.
- Hoang, T., Verma, S., Ma, S., Fister, T.T., Timoshenko, J., Frenkel, A.I., Kenis, P., and Gewirth, A.A. (2018). Nano porous copper-silver alloys by additive-controlled electrodeposition for the selective electroreduction of CO₂ to ethylene and ethanol. *J. Am. Chem. Soc.* 140, 5791–5797.
- Li, X., Bi, W., Chen, M., Sun, Y., Ju, H., Yan, W., Zhu, J., Wu, X., Chu, W., Wu, C., et al. (2017). Exclusive Ni-N4 sites realize near-unity CO selectivity for electrochemical CO₂ reduction. *J. Am. Chem. Soc.* 139, 14889–14892.
- Jiao, J.Q., Lin, R., Liu, S., Cheong, W.C., Zhang, C., Chen, Z., Pan, Y., Tang, J., Wu, K., Hung, S.F., et al. (2019). Copper atom-pair catalyst anchored on alloy nanowires for selective and efficient electrochemical reduction of CO₂. *Nat. Chem.* <https://doi.org/10.1038/s41557-018-0201-x>.
- Sharma, P.P., Wu, J., Yadav, R.M., Liu, M., Wright, C.J., Tiwary, C.S., Yakobson, B.I., Lou, J., Ajayan, P.M., and Zhou, X.D. (2015). Nitrogen-doped carbon nanotube arrays for high-efficiency electrochemical reduction of CO₂: on the understanding of defects, defect density, and selectivity. *Angew. Chem. Int. Ed.* 54, 13701–13705.
- Ye, G., Gong, Y., Lin, J., Li, B., He, Y., Pantelides, S.T., Zhou, W., Vajtai, R., and Ajayan, P.M. (2016). Defects engineered monolayer MoS₂ for improved hydrogen evolution reaction. *Nano Lett.* 16, 1097–1103.
- Jiang, H., He, Q., Li, X., Su, X., Zhang, Y., Chen, S., Zhang, S., Zhang, G., Jiang, J., Luo, Y., et al. (2019). Tracking structural self-reconstruction and identifying true active sites toward cobalt oxychloride precatalyst of oxygen evolution reaction. *Adv. Mater.* 31, e1805127.
- Huang, H., Ma, L., Tiwary, C.S., Jiang, Q., Yin, K., Zhou, W., and Ajayan, P.M. (2017). Worm-shape Pt nanocrystals grown on nitrogen-doped low-defect graphene sheets: highly efficient electrocatalysts for methanol oxidation reaction. *Small* 13, 1603013.
- Resasco, J., Chen, L.D., Clark, E., Tsai, C., Hahn, C., Jaramillo, T.F., Chan, K., and Bell, A.T. (2017). Promoter effects of alkali metal cations on the electrochemical reduction of carbon dioxide. *J. Am. Chem. Soc.* 139, 11277–11287.
- Resasco, J., Lum, Y., Clark, E., Zeledon, J.Z., and Bell, A.T. (2018). Effects of anion identity and concentration on electrochemical reduction of CO₂. *ChemElectroChem* 5, 1064–1072.
- Liu, P., and Zheng, N. (2018). Coordination chemistry of atomically dispersed catalysts. *Natl. Sci. Rev.* 5, 636–638.
- Dunwell, M., Yan, Y., and Xu, B. (2017). In situ infrared spectroscopic investigations of pyridine-mediated CO₂ reduction on Pt electrocatalysts. *ACS Catal.* 7, 5410–5419.
- Deng, H., Grunder, S., Cordova, K.E., Valente, C., Furukawa, H., Hmadeh, M., Gándara, F., Whalley, A.C., Liu, Z., and Asahina, S. (2012). Large-pore apertures in a series of metal-organic frameworks. *Science* 336, 1018–1023.
- Long, J.R., and Yaghi, O.M. (2009). The pervasive chemistry of metal-organic frameworks. *Chem. Soc. Rev.* 38, 1213.
- Batten, S.R., Champness, N.R., Chen, X.-M., Garcia-Martinez, J., Kitagawa, S., Öhrström, L., O'Keeffe, M., Paik Suh, M., and Reedijk, J. (2013). Terminology of metal-organic frameworks and coordination polymers (IUPAC Recommendations 2013). *Pure Appl. Chem.* 85, 1715–1724.
- Zhou, H.-C., Long, J.R., and Yaghi, O.M. (2012). Introduction to metal-organic frameworks. *Chem. Rev.* 112, 673–674.
- Rosen, B.A., and Hod, I. (2018). Tunable molecular-scale materials for catalyzing the low-overpotential electrochemical conversion of CO₂. *Adv. Mater.* 30, e1706238.

40. Kornienko, N., Zhao, Y., Kley, C.S., Zhu, C., Kim, D., Lin, S., Chang, C.J., Yaghi, O.M., and Yang, P. (2015). Metal-organic frameworks for electrocatalytic reduction of carbon dioxide. *J. Am. Chem. Soc.* **137**, 14129–14135.
41. Zhao, C., Dai, X., Yao, T., Chen, W., Wang, X., Wang, J., Yang, J., Wei, S., Wu, Y., and Li, Y. (2017). Ionic exchange of metal-organic frameworks to access single nickel sites for efficient electroreduction of CO₂. *J. Am. Chem. Soc.* **139**, 8078–8081.
42. Kumar, R.S., Kumar, S.S., and Kulandainathan, M.A. (2012). Highly selective electrochemical reduction of carbon dioxide using Cu based metal organic framework as an electrocatalyst. *Electrochem. Commun.* **25**, 70–73.
43. Dou, S., Song, J., Xi, S., Du, Y., Wang, J., Huang, Z.F., Xu, Z.J., and Wang, X. (2019). Boosting electrochemical CO₂ reduction on metal-organic frameworks via ligand doping. *Angew. Chem. Int. Ed.* **58**, 4041.
44. Albo, J., Vallejo, D., Beobide, G., Castillo, O., Castaño, P., and Irabien, A. (2016). Copper-based metal-organic porous materials for CO₂ electrocatalytic reduction to alcohols. *ChemSusChem* **10**, 1100–1109.
45. Hinogamiz, R., Yotsuhashi, S., Deguchi, M., Zenitani, Y., Hashiba, H., and Yamada, Y. (2012). Electrochemical reduction of carbon dioxide using a copper rubeanate metal organic framework. *ECS Electrochem. Lett.* **7**, H17–H19.
46. Hod, I., Sampson, M.D., Deria, P., Kubiak, C.P., Farha, O.K., and Hupp, J.T. (2015). Fe-porphyrin-based metal-organic framework films as high-surface concentration, heterogeneous catalysts for electrochemical reduction of CO₂. *ACS Catal.* **5**, 6302–6639.
47. Park, K.S., Ni, Z., Côté, A.P., Choi, J.Y., Huang, R., Uriberomo, F.J., Chae, H.K., O’Keeffe, M., and Yaghi, O.M. (2006). From the cover: exceptional chemical and thermal stability of zeolitic imidazolate frameworks. *Proc. Natl. Acad. Sci. U S A* **103**, 10186–10191.
48. Wang, Y.R., Huang, Q., He, C.T., Chen, Y., Liu, J., Shen, F.C., and Lan, Y.Q. (2018). Oriented electron transmission in polyoxometalate-metalloporphyrin organic framework for highly selective electroreduction of CO₂. *Nat. Commun.* **9**, 4466.
49. Baruch, M.F., Pander, J.E., White, J.L., and Bocarsly, A.B. (2015). Mechanistic insights into the reduction of CO₂ on tin electrodes using in situ ATR-IR spectroscopy. *ACS Catal.* **5**, 3148–3156.
50. Innocent, B., Pasquier, D., Ropital, F., Hahn, F., Léger, J.M., and Kokoh, K.B. (2010). FTIR spectroscopy study of the reduction of carbon dioxide on lead electrode in aqueous medium. *Appl. Catal. B* **94**, 219–224.